Hybridization of plasmon modes in multishell bimetallic nanoparticles: a numerical study

Fatema Alali,[a] Innem V. A. K. Reddy,[b,c,*] Edward P. Furlani,[b,d] and Josep M. Jornet[e]

[a]Public Authority for Applied Education and Training, College of Technological Studies, Department of Electronic Engineering, Kuwait City, Kuwait

[b]University at Buffalo SUNY, Department of Electrical Engineering, Buffalo, New York, United States

[c]King Abdullah University of Science and Technology, Biological and Environmental Science and Engineering Division, Saudi Arabia

[d]University at Buffalo SUNY, Department of Chemical and Biological Engineering, Buffalo, New York, United States

[e]Northeastern University, Department of Electrical and Computer Engineering, Boston, Massachusetts, United States

Abstract. We study the near-infrared properties of spherical multishell nanoparticles comprising a loss-less dielectric core enclosed by a concentric layering of metallic–dielectric–metallic nanoshells. The coupling between the metallic shells induces plasmon resonance redshifts and peak splitting in the absorption spectra of the layered particle relative those of the metallic constituents. We use full-wave electromagnetic analysis to investigate changes in the absorption spectra as a function of key parameters including the material properties of the inner and outer metallic shells and the aspect ratio of their inner and outer radii. We systematically vary the aspect ratios and quantify the degree of plasmonic coupling between the metallic nanoshells. Our analysis reveals conditions under which the spectral resonance peaks blueshift and/or redshift. We consider bimetallic particles with gold and silver nanoshells and determine the dependency of plasmon resonance peak shifting and splitting as a function of the order of these material layers, i.e., as inner or outer shells.
[DOI: 10.1117/1.JNP.14.036007]

Keywords: plasmonics; bimetallic nanoshells; hybrid modes.

Paper 20044 received May 4, 2020; accepted for publication Jul. 23, 2020; published online Aug. 6, 2020.

1 Introduction

Plasmonic nanostructures have attracted broad interest in recent years reflecting a proliferation of applications, especially as theranostic agents in biomedicine,[1–6] that exploit the unique optical properties of these structures, notably localized surface plasmon resonance (LSPR). LSPR is one of the most interesting features of subwavelength noble metal (Au and Ag) nanoparticles (NPs). When a plasmonic NP is illuminated with radiation at the LSPR wavelength (λ_{LSPR}), conduction electrons within the NP oscillate coherently that gives rise to a highly localized electric field accompanied by a resonance peak in the absorption spectrum.[7–10] LSPR is highly dependent on the size and shape of the NP, which can be controlled during synthesis to tune λ_{LSPR} to lie within the ultraviolet (UV) to the near-infrared region (NIR) spectral range.

Noble metal nanospheres (NSps) have been studied extensively, typically with diameters in the range of 2 to 100 nm.[5,11] The LSPR of an NSp depends on the dominant multipole order that is excited, which, in turn, is a function of its size relative to the incident wavelength, material properties, and the refractive index of the surrounding medium. It is well-known that Au NSps immersed in water ($n_{\mathrm{water}} = 1.33$) exhibit resonance in the range of 510 to 550 nm within the

*Address all correspondence to Innem V. A. K. Reddy, E-mail: innemven@buffalo.edu

1934-2608/2020/$28.00

visible spectrum.[5,11–13] For many applications, it is desirable to tune LSPR to a given spectral window. This is especially true for plasmon-based biomedical applications, e.g., photodynamic and photothermal cancer therapy (PCT), where NPs with an LSPR within the NIR "Biological Window" (800 to 1200 nm) are most effective as light at these wavelengths has a deeper penetration into human tissue relative to other wavelengths.[14–19]

The LSPR of an NPs can be tuned to the NIR using core-shell particles (CSPs)[14,20] consisting of a dielectric core enclosed in a metallic shell. Plasmon excitation arises on both the inner and outer surfaces of the shell. The outer and inner modes of the CSP correspond to a solid NSp and spherical nanovoid (NV) LSPR, respectively, where $\lambda_{\mathrm{NSp}} > \lambda_{\mathrm{NV}}$. The hybridization between NSp and NV plasmon modes causes a significant redshift (RS) in the absorption spectrum of a CSP as compared to the NSps. In other words, a CSP with a thinner shell will exhibit stronger interactions between NSp and NV modes, i.e., a greater RS, whereas the NSps plasmon modes are dominant for a thicker shell.[1,2,21,22] In addition, CSP plasmon modes depend on the refractive indices of two dielectrics: the surrounding medium (n_s) and the core (n_c). Knowing that a high refractive index RSs the LSPR, n_s and n_c can be used to control the shifts of the individual plasmon resonances λ_{NSp} and λ_{NV}, respectively. Hence, by proper tuning of n_s and n_c the difference between λ_{NSp} and λ_{NV} can be reduced to achieve a stronger hybridization between NSp and NV plasmon modes.[3,4,23,24] However, for biomedical applications, the variation of n_s is limited as the particles are generally surrounded by tissue (water). At the same time, the refractive index n_c of the core is bounded by ~1.4. Thus, the LSPR of CSPs can most effectively be tuned by controlling the inner and outer radii of the metallic shell during synthesis. The aspect ratio r for CSPs is defined as $r = a/b$, where a and b are the inner and outer radii of the shell, respectively [Fig. 1(a)]. For thick metallic shells (low r), the hybridization between the plasmon modes of the inner and outer surfaces is weak, and the absorption spectrum of the CSP resembles that of the NSp. In this paper, to provide a reference for our for multishell particle analysis, we explore the LSPR of CSPs wherein the particle diameter is fixed and the core size increases to increase the aspect ratio, i.e., as the aspect ratio increases, thickness of the metallic shell decreases. High aspect ratios (r value) correlate with a higher degree of coupling between the NSp and the NV plasmon modes, which produce a greater LSPR RS and enhanced peak splitting.[1,2] In summary, using a very thin layer of metal on a dielectric core helps in peak splitting and thereby an RS in the absorption spectrum. However, synthesis of such particles is complex as one has to precisely control the shell thickness in the range of nanometers.

Theoretical and experimental studies have shown that the factors that affect the LSPR of a CMSP [Fig. 1(b)] include the optical properties of the constituent materials, i.e., the core, dielectric shell, metallic shells, and surrounding medium, as well as the coupling of the inner and outer metallic shells, which, in turn, depends on the separation between CSP_1 and CSP_2 (coupling factor r_T). As r_T increases, the separation decreases, which results in stronger coupling between CSP_1 and CSP_2. This, in turn, gives rise to a larger LSPR RS in the CMSP absorption spectrum. This is also strongly influenced by the dielectric refractive indices in the system. The dielectrics will shift the resonances of four plasmon modes: λ_{NSp1}, λ_{NV1}, λ_{NSp2}, and λ_{NV2}. The hybridization strength depends on matching of these four resonances.[1,2,25] As we can see, the multilayer structure provides more degrees of freedom to tune the hybridization modes of the particle.

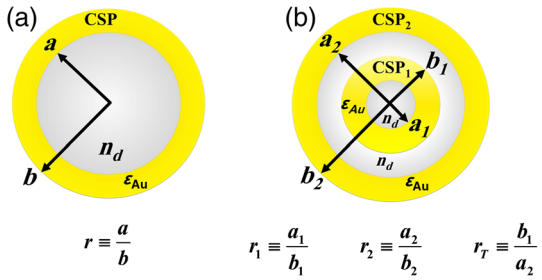

Fig. 1 (a) CSP (gold shell with a dielectric sphere) and (b) core-multishell particle (two CSPs separated by dielectric material with RI n_d). The corresponding aspect ratios are described under the figure.

In this paper, we perform a systematic numerical study of the absorption spectra of two distinct nanostructures: CSPs – dielectric–metallic (gold and silver) core-shell NPs and CMSPs – dielectric–metallic–dielectric–metallic NPs. Utilizing wave optics and RF modules from COMSOL Multiphysics, we built a model for computing CSPs and CMSPs absorption spectra. We investigate spectra variations for CSP and CMSP taking into account their aspect ratios and metallic materials properties. After we fix b_2 at 50 nm, the geometric parameters r_1, r_2, and r_T are chosen independently, where their range is between 0 and 1. By setting these individual parameters, the dimensions of a_2, b_1, and a_1 follow from parameter definitions as shown in Fig. 1(b). We show that r_1 and r_2 directly affect the minimum r_T required for CSP_1 and CSP_2 coupling. Moreover, we highlight conditions for blue shift (BS) and/or RS of the split resonance peaks that occur due to coupling between CSP_1 and CSP_2. From the geometric parameters of the constituent nanostructures (r_1 and r_2 for CSP_1 and CSP_2, respectively), we obtain a general view of the spectral changes for the entire particle (LSPR shifts are accommodated with a spectral peak split). Finally, we illustrate the advantages of using bimetallic Au and Ag CMSPs as they provide a larger parameter space to achieve more robust spectral tuning. Four combinations are possible for the CMSP structure, two are monometallic (Au–Au and Ag–Ag), and two bimetallic (Au–Ag and Ag–Au) inner and outer metallic shells. However, we present results for a subset of the bimetallic with Au as the outer shell, i.e., Ag–Au due to the advantages and disadvantages mentioned above for Au and Ag NPs. We use heat transfer module of COMSOL to investigate the volume average of temperature for bimetallic CMSPs and show that the NIR absorption peak of bimetallic Ag–Au CMSP is higher than the one for Au–Au for the same heating source, which makes Ag–Au CMSPs a better choice for photothermal applications.

2 Computational Model

We investigate the optical properties of the select plasmonic nanostructures using full wave time-harmonic field theory. We use the COMSOL Multiphysics software for the analysis. A representative computational domain is shown in Fig. 2(a). A single CMSP as shown in Fig. 2(b) is centered at the origin of the domain. The geometry of this particle is defined by the three aspect ratios as shown in Fig. 1: $r_1 = a_1/b_1$, $r_2 = a_2/b_2$, and $r_T = b_1/a_2$, with $b_2 = 50$ nm. We fix the particle size b_2 to suppress multipole excitation due to retardation effects.[21] The particle is illuminated with a uniform downward-directed plane wave whose electric field E is parallel to the x axis. Perfectly matched layers (PMLs) are applied at the top and bottom of the domain to reduce back scatter from these boundaries. Perfect electric conductor and perfect magnetic conductor conditions are applied at the boundaries perpendicular to E and to the magnetic field H, respectively. These symmetry boundary conditions mimic the response of a two-dimensional array of identical particles with a center-to-center x and y lattice spacing equal to the width of the computational domain in the x and y directions, respectively. The lattice spacing was

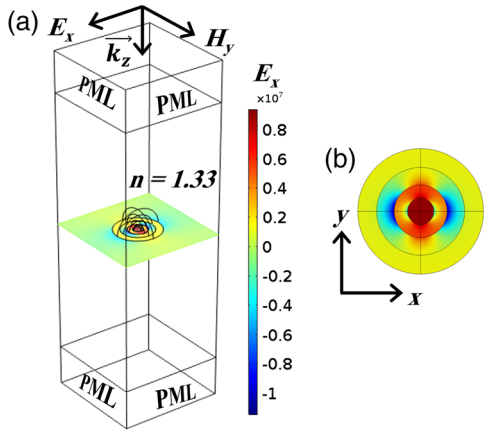

Fig. 2 (a) Computational domain with CMSP within H_2O (RI = 1.33). PMLs are placed on top and bottom of rectangular domain. (b) Hybridized plasmon resonance in CMSP.

chosen to be sufficiently large so that the predictions reflect the response of a single isolated particle, i.e., with negligible coupling with neighboring particles. The time-harmonic E field within the domain satisfies the equation:

$$\nabla \times (\mu_r^{-1} \nabla \times \mathbf{E}) - k_0^2 \left(\epsilon_r - j \frac{\sigma}{\omega \epsilon_0} \right) \mathbf{E} = 0, \tag{1}$$

where μ_r and ϵ_r are the relative permeability and permittivity of the media, respectively. In the case of the CMSP shown in Fig. 1, we use $\mu_r = 1$ for the metallic shells CSP_1 and CSP_2 whereas ϵ_r is obtained from the Drude model for Au[26,27] and Ag.[28–31] For the CMSP dielectric constituents (core and shell), we use $n_c = 1.4$. The fluid surrounding the CMSP is assumed to be non-absorbing water with $n_{\text{water}} = 1.33$. The incident field is generated by a time-harmonic surface current positioned in the XY-plane directly below the upper PML.[18]

COMSOL RF module is coupled with the heat transfer module to analyze the temperature of a CMSP. The heat transfer module uses the equation

$$\rho C_p \frac{\partial T}{\partial t} + \nabla \cdot (-k \nabla t) = Q, \tag{2}$$

where Q is the heat source, ρ is the heat density, C_p is the specific heat capacity, and k is the thermal conductivity of the material. Here, the heat source is taken as total power dissipation density Q_h and is fed from the RF module.

3 Results

In this section, we provide a detailed discussion of the absorption spectra of the CSPs and CMSPs in that order. The structure for CSP and CMSP is shown in Figs. 1(a) and 1(b), respectively. In CMSPs, the aspect ratios and the material of metallic shells are varied and analyzed in a systematic manner.

3.1 *Monoshell Structures*

As we discussed above, a CSP contains a dielectric core with metal coating. The refractive index of core is 1.4 while the refractive index of surrounding medium is 1.33. The absorption spectra is computed parametrically as a function of the aspect ratio $r = a/b$, where a and b are the inner and outer radii of the shell. For this analysis, the particle size is fixed, $b = 50$ nm, whereas r is varied from 0.5 to 0.8. In Fig. 3(a), we compare our numerical observations with the analytical results. The analytical results are plotted with the help of models developed by Zhu et al.[25] and Khosravi et al.[32] The analytical models are based on a quasistatic approach. We used MATLAB to plot the results. Normalized absorption spectra for both Au and Ag CSPs are shown in Fig. 3(b). For smaller r, i.e., thicker shells, the peak splitting in the spectra (i.e., the appearance

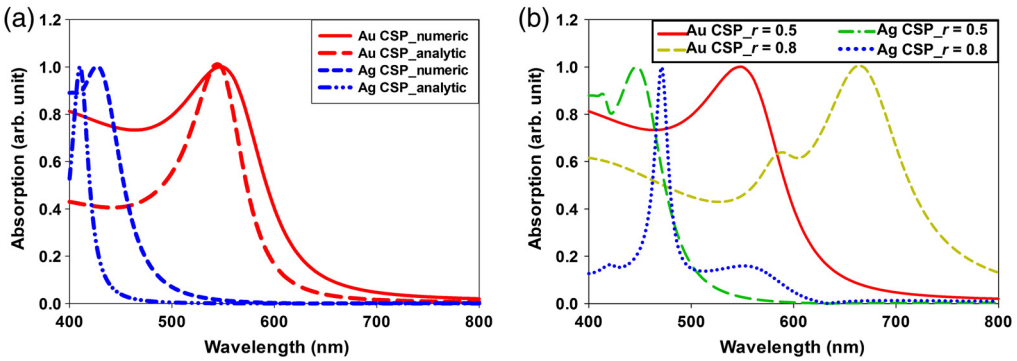

Fig. 3 (a) Numeric versus analytic results for Au and Ag CSPs with $r = 0.5$. (b) Normalized absorption spectra of Au and Ag CSPs for $r = 0.5$ and 0.8 (numerical results).

of multiple local maxima) is not dominant, whereas for larger r the peaks split and the dominant (global maximum) resonant peak is redshifted. We find that for a low aspect ratio, the Au CSP has an LSPR near 550 nm, but as the aspect ratio increases, this resonance shifts toward 660 nm. This is due to the interaction between NV and NSp plasmon modes. A similar effect is observed for the Ag CSP. Silver exhibits resonance in the UV region and can be shifted to visible by increasing the aspect ratio.

These results are consistent with published data.[1,2] Although the Ag and Au CSPs exhibit a pronounced resonance, their spectral peaks are not in the NIR region, which, as noted, is crucial for many biomedical applications. To shift the peak to the NIR, the aspect ratio must be as high as 0.9 for Au CSP leading to a very thin metal coating. Moreover, this will result in a broad resonance peak, which is not ideal. An alternate way to generate narrow LSPR resonance peaks is via CMSPs as shown in the following.

3.2 *Multiple Shell Structures*

The CMSPs that we consider consist of two metallic nanoshells separated by a dielectric shell layer [as shown in Fig. 1(b)]. In this paper, the CMSPs can be mono- or bimetallic, i.e., the two metallic shells can be the same or different metals. For simplicity, we consider similar aspect ratios for both shells i.e., $r_1 = r_2$. Another important parameter that impacts the plasmonic coupling is the interaction between the metallic shells CSP_1 and CSP_2 and is represented by the coupling factor r_T. In general, the CMSP absorption spectrum exhibits two peaks when there is appreciable coupling between CSP_1 and CSP_2; λ_{BS} and λ_{RS} are wavelengths of the first and second peaks. We present the following data to quantify the hybridization of the plasmon response: the LSPR wavelengths of the single shells, λ_{CSP1} and λ_{CSP2} and the separation between the two peaks, $\Delta\lambda_{CMSP}$; the difference between the absorption spectrum LSPRs of the outer shell and the first and second peaks, $\Delta\lambda_{BS}$ and $\Delta\lambda_{RS}$, respectively; and the minimum r_T required for CSP_1 and CSP_2 coupling, i.e., the first r_T that exhibits peak splitting. The coupling between CSP_1 and CSP_2 is manifest in the CMSP absorption spectrum as peak splitting of the LSPR corresponding to CSP_2.[1,2] The splitting results in two peaks: one with a BS and the other with a RS with respect to the CSP_2 resonance peak. However, the peak separation between the BS and RS increases with increasing coupling (r_T) between CSP_1 and CSP_2. In the following sections, we categorized CMSP as monometallic and bimetallic.

3.2.1 *Monometallic structures*

In this section, both the nanoshells are made of gold (Au) or silver (Ag) and we fix the individual aspect ratios r_1 and r_2; further, we vary the coupling factor r_T from weak to strong coupling ($r_T = 0.2$ and 0.8) and calculate the absorption spectra of the corresponding CMSPs. We use different values for r_1 and r_2 ($r_1 = r_2 = 0.5$ and 0.7) and present our results in Tables 1 and 2 for Au–Au and Ag–Ag CMSPs, respectively. The comparison between the numeric and analytic results for the monometallic CMSPs are shown in Fig. 4, and Figs. 5(a) and 5(b) show the normalized absorption spectra of the Au–Au and Ag–Ag CMSPs, respectively, with $r_1 = r_2 = 0.5$ and 0.7. Comparing Figs. 5(a) and 5(b), we see that the coupling between CSP_1 and CSP_2 depends on their individual aspect ratios (r_1 and r_2) in addition to the dielectric thickness

Table 1 Absorption characteristics of Au–Au CMSPs with equal aspect ratios for outer and inner CSPs.

Case	λ_{CSP1} (Au) (nm)	λ_{CSP2} \(Au) (nm)	Minimum r_T for coupling	λ_{BS} for $r_T = 0.8$ (nm)	λ_{RS} for $r_T = 0.8$ (nm)	$\Delta\lambda_{BS}$ $\lvert\lambda_{CSP2} - \lambda_{BS}\rvert$ (nm)	$\Delta\lambda_{RS}$ $\lvert\lambda_{RS} - \lambda_{CSP2}\rvert$ (nm)	$\Delta\lambda_{CMSP}$ ($\lambda_{RS} - \lambda_{BS}$) (nm)
$r_1 = r_2 = 0.5$	550	550	0.5	530	760	20	210	230
$r_1 = r_2 = 0.6$	570	570	0.4	540	820	30	250	280
$r_1 = r_2 = 0.7$	600	600	0.2	550	915	50	315	365

Table 2 Absorption characteristics of Ag–Ag CMSPs with equal aspect ratios for outer and inner CSPs.

Case	λ_{CSP1} (Ag) (nm)	λ_{CSP2} (Ag) (nm)	Minimum r_T for coupling	λ_{BS} for $r_T = 0.8$ (nm)	λ_{RS} for $r_T = 0.8$ (nm)	$\Delta\lambda_{BS}$ $\lvert\lambda_{CSP2} - \lambda_{BS}\rvert$ (nm)	$\Delta\lambda_{RS}$ $\lvert\lambda_{RS} - \lambda_{CSP2}\rvert$ (nm)	$\Delta\lambda_{CMSP}$ $(\lambda_{RS} - \lambda_{BS})$ (nm)
$r_1 = r_2 = 0.5$	430	430	0.5	388	672	42	242	284
$r_1 = r_2 = 0.6$	444	444	0.4	390	735	54	291	345
$r_1 = r_2 = 0.7$	485	485	0.3	398	830	70	345	432

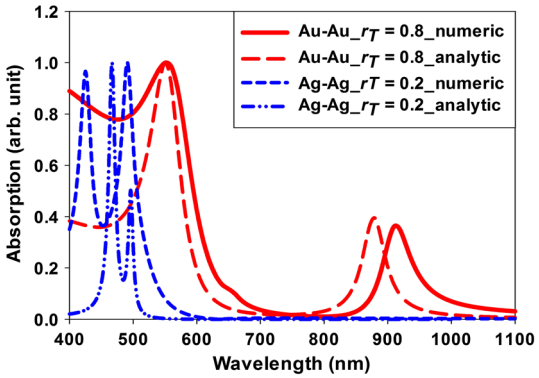

Fig. 4 Numeric versus analytic results for Au–Au and Ag–Ag CMSPs with $r_1 = r_2 = 0.7$.

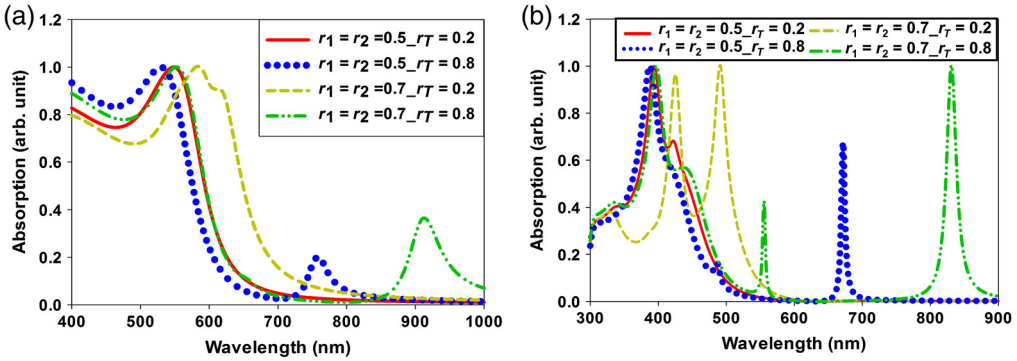

Fig. 5 (a) Normalized absorption spectra of Au–Au CMSP with varying aspect ratio $r_1 = r_2 = 0.5$ and 0.7 and coupling factor $r_T = 0.2$ and 0.8. A steady RS in the resonant peaks can be observed as the aspect ratio and coupling factor increase. (b) Normalized absorption spectra of Ag–Ag CMSP for aspect ratios $r_1 = r_2 = 0.5$ and 0.7 and coupling factor $r_T = 0.2$ and 0.8. Similar to Au–Au CMSP, there is a steady RS although the rate of shift is considerably low in Ag–Ag CMSP.

between them, which we characterized by r_T. As the aspect ratio becomes larger or as thickness of the metal decreases, peak splitting can be observed and the RS of the resonant peak is predominant. Resonance in the NIR can be achieved given a sufficiently high aspect ratio and coupling factor. The RS is greater for the Au–Au as compared to the Ag–Ag CMSPs, given the same aspect ratio. The same can be seen in Tables 1, wherein we also characterized the RS with respect to the single shell CSP. We also found that the separation between absorption peak increases as the aspect ratio increases and is greater for the Au–Au as compared to the Ag–Ag CMSPs. As shown in Tables 1 and 2, even in cases where a large separation exists between CSP_1 and CSP_2 (low $r_T = 0.2$), coupling can occur for high-aspect-ratio shells ($r_1 = r_2 = 0.7$). In fact, both

Tables 1 and 2 show that the minimum r_T required for coupling decreases as r_1 and r_2 increase.

Monometallic CMSPs are used for photothermal bio applications. We predict that the amplitude of the normalized absorption is less for the Au–Au at λ_{RS} as compared to Ag–Ag CMSPs. In other words, a higher incident irradiance is needed to achieve the same photothermal (transduction) temperature increase with the gold-based as compared to silver-based particles. However, in general, silver is not preferred for photothermal applications due to its biocompatibility and oxidizing properties.[33–35] Hence, there is a need for different particle structure that yield a similar RS with enhanced photothermal efficiency. This can be achieved using bimetallic CMSPs.[36]

3.2.2 *Bimetallic structures*

In this case, the inner metallic shell is made of silver (Ag) and outer is made of gold (Au). We perform a similar analysis as above for the monometallic CMSPs. We use Ag for the inner shell and Au for the outer because of the superior biocompatibility and oxidizing properties of gold. We demonstrate that bimetallic CMSPs are absorption and RS advantaged with respect to monometallic Au–Au and Ag–Ag CMSPs, respectively. Similar to monometallic CSMPs, in bimetallic CMSPs the plasmons of one of the metallic shells interact with plasmons of other metallic shell, thereby generating hybridized plasmon modes. These modes for the CMSP arise from the interactions among four plasmon modes on the outer and inner surfaces of CSP_1 and CSP_2. After we compare our numeric results for Ag–Au CMSP to the analytic ones [Fig. 6(a)], we show the modes interaction evidence (peak splitting) in Ag–Au CMSP in Fig. 6(b). Table 3 shows similar analysis for the bimetallic CMSPs. For high aspect ratios, the peak splitting and the results shown in Table 3 follow the same trend as for monometallic CMSPs. There is an increase in RS as the aspect ratio increases and thereby a decrease in the coupling factor. This is clearly shown in Fig. 7(a) where we plot the RS peak (λ_{RS}) as function in $r_1 = r_2$. For lower aspect ratios

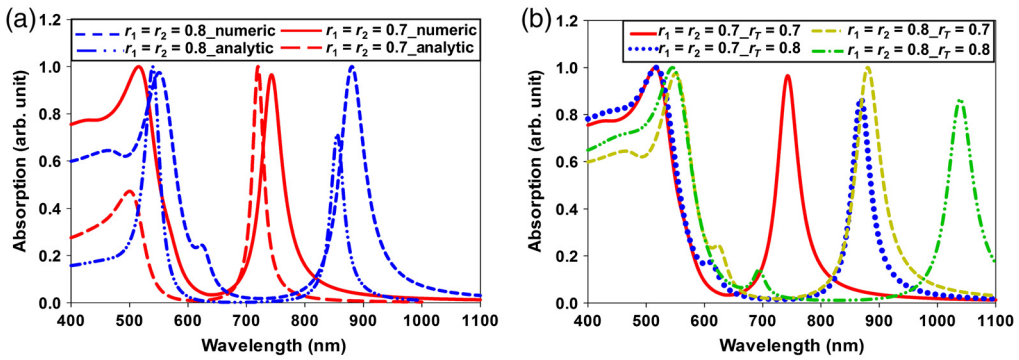

Fig. 6 (a) Numeric versus analytic results for Ag–Au CMSPs with $r_T = 0.7$. (b) Normalized absorption spectra of bimetallic CMSP (Ag–Au CMSP) with varying aspect ratio ($r_1 = r_2 = 0.7$ and 0.8) and coupling factor ($r_T = 0.7$ and 0.8). Very rich resonance peaks can be observed in the NIR region.

Table 3 Absorption characteristics of Ag–Au CMSPs with equal aspect ratios for outer and inner CSPs.

Case	λ_{CSP1} (Ag) (nm)	λ_{CSP2} (Au) (nm)	Minimum r_T for coupling	λ_{BS} for $r_T = 0.8$ (nm)	λ_{RS} for $r_T = 0.8$ (nm)	$\Delta\lambda_{BS}$ $\lvert\lambda_{CSP2} - \lambda_{BS}\rvert$ (nm)	$\Delta\lambda_{RS}$ $\lvert\lambda_{RS} - \lambda_{CSP2}\rvert$ (nm)	$\Delta\lambda_{CMSP}$ $(\lambda_{RS} - \lambda_{BS})$ (nm)
$r_1 = r_2 = 0.5$	430	550	0.6	520	710	30	160	190
$r_1 = r_2 = 0.6$	444	570	0.5	515	770	55	200	255
$r_1 = r_2 = 0.7$	485	600	0.2	516	868	84	268	352

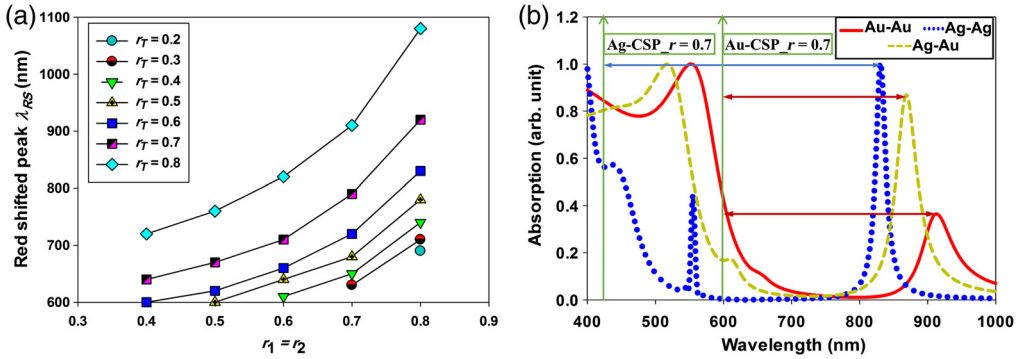

Fig. 7 (a) Minimum r_T required to manifest λ_{RS} due to peak splitting (coupling between CSP_1 and CSP_2) at different aspect ratios $r_1 = r_2$. For lower $r_1 = r_2$, peak splitting occur at higher r_T. As expected, longer λ_{RS} occurs for higher $r_1 = r_2$ and r_T, (b) normalized CMSP absorption spectra used to measure $\Delta\lambda_{RS}$ for $r_1 = r_2 = 0.7$ and $r_T = 0.8$, for monometallic and bimetallic CMPS. Vertical arrows indicate the LSPR of Au and Ag CSP with $r = 0.7$.

($r_1 = r_2 = 0.4$), λ_{RS} manifestation starts at higher coupling factor ($r_T = 0.6$). Yet, as the aspect ratios increase to 0.8, the peak splitting occurs at r_T as low as 0.2. We compare the normalized absorption spectra for the monometallic (Au–Au, Ag–Ag) CMSPs and the bimetallic (Ag–Au) with their respective outer CSPs in Fig. 7(b). The plots reveal a very rich resonance. Although the rate of RS increase for Ag–Au is lower than that of Au–Au CMSP, there is a substantial growth in absorption when the CMSP is bimetallic. Adding an Ag shell enhances the absorption but does not affect the RS. This means that similar amount of absorption can be achieved with less irradiance and in less time.

To illustrate the absolute advantage of utilizing Ag–Au CMSP in the place of Au–Au CMSP, we performed a photothermal analysis of CSPs. For this purpose, we used COMSOL's heat transfer module coupled with electromagnetics RF module. The irradiation sources are usually high power pulsed laser sources. The CMSPs discussed in the paper can be used as nanoscale heat sources for PCT and requires pulsed NIR laser sources. With the advancements in laser industry, there are a wide variety of high power solid-state and fiber lasers[37] that are finding ways into medicine, particularly to diagnose and treat cancer. In this model, the incident laser source leads to the absorption in NPs and this in return acts as a heat source. We chose the model with $r_1 = r_2 = 0.7$ and $r_T = 0.8$. In this configuration, resonance for Ag–Au is observed to be at 868 nm while Au–Au is observed to be at 915 nm. One can observe a maximum temperature rise at the resonant wavelengths, and hence we performed analysis at these resonant wavelengths. From Fig. 8, the volume average of temperature shows a gradual increase for Ag–Au when compared to Au–Au CMSP. We can achieve a temperature rise of 60K in less time if we opt Ag–Au in the place of Au–Au. These observations are consistent with previous observations.[38,39] Figures 7(b) and 8 show a clear advantage of choosing bimetallic over monometallic CMSP. It

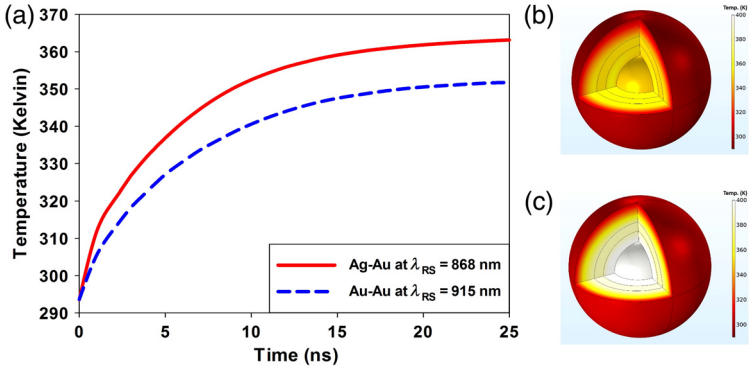

Fig. 8 (a) Temperature increase as a function in time for Ag–Au and Au–Au CMSPs. The three-dimensional plot shows heat distribution for Ag–Au CMSPs at (b) 5 ns and (c) 25 ns.

overcomes the limitations posed by Ag–Ag CMSP as well as Au–Au CMSP. Hence, using bimetallic CMSPs opens up new possibilities for flexible and efficient theranostic bioapplications, specifically PCT. PCT has emerged over the years as a potential replacement for chemotherapy, a conventional cancer treatment technique. Although PCT offers substantially low side-effects, it requires highly efficient NPs with a narrow absorption peak.[40] Using bimetallic CMSPs in the place of traditional gold and silver NPs[41] could increase the efficiency along with a narrow absorption peak. It can serve as an advancement in the field of PCT as well as offer flexibility.

4 Conclusion

We performed a systematic numerical study to investigate the plasmon hybridization as manifest in the absorption spectra of CMSPs as a function of their metallic shells, CSP_1 and CSP_2, and respective aspect ratios r_1 and r_2. We have shown that CMSPs with high r_1 and r_2 manifest plasmon hybridization at low r_T values. In both structures (mono and bimetallic), the plasmonic coupling for CMSPs strongly depends not only on the nanoshells separation factor r_T but also on the individual aspect ratios r_1 and r_2. Our results show that the bimetallic CMSP Ag–Au exhibits improved NIR shift and associated high absorption compared to the monometallic ones Ag–Ag and Au–Au CMSPs, respectively. Moreover, we apply thermal analysis for both mono- and bimetallic CMSPs and show that the photothermal transduction efficiency of the latter is enhanced in the NIR. Hence, CMSPs can provide an improved NIR absorption peaks for a local heating source. We are currently using the same procedure to investigate the spectra of porous NPs. These results will provide a general view of complex plasmon hybridization based on key geometric parameters. Although we considered spherical particles with two concentric metallic shells made of gold or silver, our modeling method readily extends to nanostructures with arbitrary shapes and material constituents. As such, it should be useful for the development and design of plasmonic NPs for a broad range of applications including theranostic agents in the field of biomedicine.

Acknowledgments

Authors would like to acknowledge Dr. A. Baev for his valuable comments and discussion. FA and IVAKR contributed equally. EPF and JMJ supervised the progress of this project. All authors reviewed the manuscript. The authors declare no competing interests. The authors declare no conflicts of interest related to this article

References

1. E. Prodan et al., "A hybridization model for the plasmon response of complex nanostructures," *Science* **302**(5644), 419–422 (2003).
2. E. Prodan and P. Nordlander, "Plasmon hybridization in spherical nanoparticles," *J. Chem. Phys.* **120**(11), 5444–5454 (2004).
3. J. L. West and N. J. Halas, "Engineered nanomaterials for biophotonics applications: improving sensing, imaging, and therapeutics," *Annu. Rev. Biomed. Eng.* **5**, 285–292 (2003).
4. N. J. Halas, "Playing with plasmons. Tuning the optical resonant properties of metallic nanoshells," *MRS Bull.* **30**(5), 362–367 (2005).
5. J. Z. Zhang, "Biomedical applications of shape-controlled plasmonic nanostructures: a case study of hollow gold nanospheres for photothermal ablation therapy of cancer," *J. Phys. Chem. Lett.* **1**(4), 686–695 (2010).
6. T. Shahar, T. Sicron, and D. Mandler, "Nanosphere molecularly imprinted polymers doped with gold nanoparticles for high selectivity molecular sensors," *Nano Res.* **10**(3), 1056–1063 (2017).
7. S. Link and M. A. El-Sayed, "Shape and size dependence of radiative, non-radiative and photothermal properties of gold nanocrystals," *Int. Rev. Phys. Chem.* **19**(3), 409–453 (2000).

8. K. L. Kelly et al., "The optical properties of metal nanoparticles: the influence of size, shape, and dielectric environment," *J. Phys. Chem. B* **107**(3), 668–677 (2003).
9. L. M. Liz-Marzan, "Tailoring surface plasmons through the morphology and assembly of metal nanoparticles," *Langmuir* **22**(1), 32–41 (2006).
10. M. A. El-Sayed, "Small is different: shape-, size-, and composition-dependent properties of some colloidal semiconductor nanocrystals," *Acc. Chem. Res.* **37**(5), 326–333 (2004).
11. M. Hu et al., "Gold nanostructures: engineering their plasmonic properties for biomedical applications," *Chem. Soc. Rev.* **35**(11), 1084–1094 (2006).
12. P. K. Jain and M. A. El-Sayed, "Plasmonic coupling in noble metal nanostructures," *Chem. Phys. Lett.* **487**(4-6), 153–164 (2010).
13. P. K. Jain et al., "Calculated absorption and scattering properties of gold nanoparticles of different size, shape, and composition: applications in biological imaging and biomedicine," *J. Phys. Chem. B* **110**(14), 7238–7248 (2006).
14. S. J. Oldenburg et al., "Nanoengineering of optical resonances," *Chem. Phys. Lett.* **288**(2-4), 243–247 (1998).
15. N. Harris et al., "Tunable infrared absorption by meta nanoparticles: the case for gold rods and shells," *Gold Bull.* **41**(1), 5–14 (2008).
16. L. F. Gou and C. J. Murphy, "Fine-tuning the shape of gold nanorods," *Chem. Mater.* **17**(14), 3668–3672 (2005).
17. J. Y. Chen et al., "Gold nanocages as photothermal transducers for cancer treatment," *Small* **6**(7), 811–817 (2010).
18. I. H. Karampelas et al., "Plasmonic nanoframes for photothermal energy conversion," *J. Phys. Chem. C* **120**(13), 7256–7264 (2016).
19. C. R. Simpson et al., "Near-infrared optical properties of *ex vivo* human skin and subcutaneous tissues measured using the Monte Carlo inversion technique," *Phys. Med. Biol.* **43**(9), 2465–2478 (1998).
20. A. E. Neeves and M. H. Birnboim, "Composite structures for the enhancement of nonlinear-optical susceptibility," *J. Opt. Soc. Am. B* **6**(4), 787–796 (1989).
21. D. Sarid and W. A. Challener, *Modern Introduction to Surface Plasmons: Theory, Mathematical Modeling, and Applications*, Cambridge University Press, Cambridge; New York (2010).
22. D. W. Brandl and P. Nordlander, "Plasmon modes of curvilinear metallic core/shell particles," *J. Chem. Phys.* **126**(14) (2007).
23. C. Loo et al., "Immunotargeted nanoshells for integrated cancer imaging and therapy," *Nano Lett.* **5**(4), 709–711 (2005).
24. D. P. O'Neal et al., "Photo-thermal tumor ablation in mice using near infrared-absorbing nanoparticles," *Cancer Lett.* **209**(2), 171–176 (2004).
25. J. Zhu, Y. J. Ren, and S. M. Zhao, "Refractive index sensitivity of gold double concentric nanoshells: tuning the intensity discrepancy of two-band plasmonic absorption," *Sens. Actuators B* **161**(1), 1129–1134 (2012).
26. P. G. Etchegoin, E. C. Le Ru, and M. Meyer, "An analytic model for the optical properties of gold," *J. Chem. Phys.* **125**(16), 164705 (2006).
27. P. G. Etchegoin, E. C. Le Ru, and M. Meyer, "An analytic model for the optical properties of gold (vol 125, pg 164705, 2006)," *J. Chem. Phys.* **127**(18), 189901 (2007).
28. V. P. Drachev et al., "The Ag dielectric function in plasmonic metamaterials," *Opt. Express* **16**(2), 1186–1195 (2008).
29. P. B. Johnson and R. W. Christy, "Optical constants of noble metals," *Phys. Rev. B* **6**(12), 4370–4379 (1972).
30. Y. J. Jiang, S. Pillai, and M. A. Green, "Re-evaluation of literature values of silver optical constants," *Opt. Express* **23**(3), 2133–2144 (2015).
31. H. H. U. Yang et al., "Optical dielectric function of silver," *Phys. Rev. B* **91**(23), 235137 (2015).
32. H. Khosravi, N. Daneshfar, and A. Bahari, "Theoretical study of the light scattering from two alternating concentric double silica-gold nanoshell," *Phys. Plasmas* **17**(5), 053302 (2010).

33. P. E. Laibinis et al., "Comparisons of self-assembled monolayers on silver and gold – mixed monolayers derived from $HS(CH_2)_{21}X$ and $HS(CH_2)_{10}Y$ (X, Y = CH_3, CH_2OH) have similar properties," *Langmuir* **7**(12), 3167–3173 (1991).
34. N. Bartlett, "Relativistic effects and the chemistry of gold," *Gold Bull.* **31**(1), 22–25 (1998).
35. P. E. Laibinis et al., "Comparison of the structures and wetting properties of self-assembled monolayers of normal-alkanethiols on the coinage metal-surfaces, Cu, Ag, Au," *J. Am. Chem. Soc.* **113**(19), 7152–7167 (1991).
36. A. Ahmadivand, R. Sinha, and N. Pala, "Resonance coupling in plasmonic nanomatryoshka homo- and heterodimers," *AIP Adv.* **6**(6), 065102 (2016).
37. M. Zhou et al., "Theranostic probe for simultaneous *in vivo* photoacoustic imaging and confined photothermolysis by pulsed laser at 1064 nm in 4t1 breast cancer model," *Nanoscale* **6**(24), 15228–15235 (2014).
38. K. Liu, X. Z. Xue, and E. P. Furlani, "A numerical study of the photothermal behaviour of near-infrared plasmonic colloids," *RSC Adv.* **6**(103), 100670–100675 (2016).
39. X. Huang and M. A. El-Sayed, "Gold nanoparticles: optical properties and implementations in cancer diagnosis and photothermal therapy," *J. Adv. Res.* **1**(1), 13–28 (2010).
40. S. Lal, S. E. Clare, and N. J. Halas, "Nanoshell-enabled photothermal cancer therapy: Impending clinical impact," *Acc. Chem. Res.* **41**(12), 1842–1851 (2008).
41. A. M. Gobin et al., "Near-infrared resonant nanoshells for combined optical imaging and photothermal cancer therapy," *Nano Lett.* **7**(7), 1929–1934 (2007).

Fatema Alali received her BE degree in electrical engineering from the Kuwait University in 1977, and her MS and PhD degrees in electrical engineering from University at Buffalo, New York, in 2004 and 2013, respectively. In 2002, she joined as a faculty in the Department of Electronic Engineering in the Public Authority for Applied Education and Training (PAAET), Kuwait. Currently, she is an assistant professor in PAAET, and her research focuses on nanophotonics.

Innem V.A.K. Reddy received his bachelor's degree from the NIT Goa, India, in 2015. Later, he pursued his MS degree in electrical engineering from UB and graduated in February 2018. Currently, he is pursuing a dual PhD, one in electrical engineering at UB under Dr. Josep Jornet and the other in the bioscience at KAUST under the supervision of Dr. Carlo Liberale. His current research interests are in 3D nanofabrication, optical tweezers, and terahertz communications.

Edward P. Furlani received his PhD from UB in 1982. He worked as a professor in the Departments of Chemical and Biological Engineering and Electrical Engineering at UB. His scientific contributions include over 100 peer-reviewed publications, 90 journal publications, and over 152 US patents. He was a member of OSA, IEEE, AICE, and a fellow at the Inventors' National Academy. His work inspired many of his students and colleagues to pursue more challenging projects.

Josep M. Jornet received his PhD in electrical and computer engineering from the Georgia Institute of Technology in August 2013, under the guidance of Professor Ian F. Akyildiz. He worked as an assistant professor in the Department of Electrical Engineering at UB from 2013 until 2019. Currently, he is an associate professor at Northeastern University. His research interests include terahertz-band communication networks, nanophotonic wireless communication, wireless nano-bio-sensing networks, and the internet of nano-things.